eJSE INTERNATIONAL

Prediction of Ultimate Strain in AFRP- Confined Concrete Columns Using Regression - Based Machine Learning Algorithms

Jingli WEN [a*]

[a] School of Urban Construction Engineering, Chongqing Technology and Business Institute, Chongqing 401520, China
*Corresponding author: xiaowen430309@126.com

Abstract

Concrete confinement using fiber-reinforced polymer (FRP) jackets is widely employed in structural retrofitting. A number of machine learning (ML) algorithms using tree-based methodologies were developed to forecast the ultimate strain (ε_{cu}) of circular columns wrapped in aramid fiber-reinforced polymer (AFRP). Hyperparameters are optimized using Artificial Hummingbird Optimizer (AHO) and Giant Trevally Optimizer (GTO) with least square support vector regression (LSSVR), leveraging AFRP-made concrete data from earlier studies to establish a suitable dataset. The AFRP jacket's total thickness (t_f), elastic modulus (E_f), ultimate tensile strength (f_f), the height of the column (L), unconfined compressive strength (f_{co}), and specimen diameter (d) are the input variables used in this approach. LSSVR(A) got the smallest uncertainty values (0.2893 and 0.2261) in training and evaluation. The values obtained during learning and evaluation were lower than LSSVR(G)'s 0.323 and 0.2476. The variation percentage between the two models for these measures, that is, at least 7% and sometimes 36%, depending on the variance percentage that was employed, shows the accuracy and reliability of the LSSVR(G). Regarding MAE index values, throughout the training and assessment stages, the LSSVR(A) achieved values of 0.0676 and 0.0559, respectively, while the LSSVR(G) received the smallest values of 0.0591 and 0.0434.

Keywords

1. Introduction

Following the implementation of FRP encapsulation to boost and rehabilitate reinforced concrete structures, comprehensive studies have been undertaken about its attributes and efficacy (Arabshahi et al., 2015; Ebrahim & Mahzad, 2024; Khorasani et al., 2019; Pham & Hao, 2016; Sabzi & Esfahani, 2018; Shaikh & Alishahi, 2019; Stylianidis & Petrou, 2019). A multitude of investigations has been undertaken to create numerical models for calculating stress and strain in constrained concrete columns, originally derived from the correlations of steel-reinforced models (Babak et al., 2024; Fardis & Khalili, 1982; Saadatmanesh et al., 1994). The linear action of FRP results in a stress-strain diagram devoid of a softening branch, with models sorted into two types: data-driven and solution-driven (Lam & Teng, 2003). The initial cluster is formulated through the implementation of progressive evaluation to attain the load-deformation crescent (Jiang & Teng, 2007; Rousakis et al., 2008; Teng et al., 2007). The subsequent type of models is refined and formulated by numerical regression utilizing prior data from experiments (Chastre & Silva, 2010; Faustino et al., 2014; Rousakis et al., 2012; Sadeghian & Fam, 2015). Solution-based models are favored for their simplicity; nevertheless, data-driven models offer superior alignment with mechanical characteristics.

Multiple methodologies exist for assessing stress and strain in FRP-reinforced concrete; however, current research is focused on enhancing their precision and application, particularly by examining the influence of laboratory sample size on 37 samples of varying dimensions (Elsanadedy et al., 2012). The empirical plan was further validated through mathematical assessments (Jiang & Teng, 2012). Jiang and Teng (2012) proposed a theoretical model for slender FRP-confined circular pillars based on the Lam and Teng stress–strain technique. Later, Nguyen et al. introduced a fresh approach after investigating the dilation acting of normal concrete confined with FRP wraps (Nguyen et al., 2018). This work shows that FRP yarn twist exhibits superior confinement performance compared to FRP sheet; (W. Wang et al., 2018) also conducted empirical investigations on round concrete columns with partial FRP confinement. A resolution-based model was developed to accurately forecast the load-deformation behavior of FRP-confined pillars. In 2014, Siddiqui et al. proposed a correlation to define the slenderness restriction for CFRP-confined concrete pillars based on empirical outputs (Siddiqui et al., 2014). In the year 2014, Pham and Hadi enhanced their strength-based methodology and introduced a focus on a solutions model for conventional and reinforced round concrete columns encased with FRP (Pham & Hadi, 2014). This innovative approach enabled a more comprehensive understanding of the behavior and structural capabilities of FRP-limited concrete colllumns, with the potential for widespread application across

various engineering disciplines. The proposed model is applicable to seven kinds of FRP substances. Zhou et al. developed a load-deformation model based on tests of FRP-confined lightweight aggregate concrete under axial loading (Zhou et al., 2016). In 2016, the pivotal conduct of round cement-based composite-occupied FRP pipes was empirically investigated by Hadi et al., taking into account the influence of eccentricity (Hadi et al.,2016). Rong and Shi enhanced a defeated standard for FRP-limited cement-based composite by utilizing the twin shear resistance hypothesis, leading to the expansion of a data-driven resistance method (Rong & Shi, 2018). Fallah Pour et al. have introduced a straightforward, solution-focused model for FRP-encased circular concrete columns that achieve an improved equilibrium between precision and simplicity (Pour et al., 2018). While most earlier investigations focused on graphite and silicate-based FRPs, recent interest has shifted toward aromatic polyamide FRPs (AFRPs) due to their superior ductility. Ozbakkaloglu and Akin showed that AFRP offers bigger plasticity than CFRP under axial loading, making it optimal for seismic applications (Ozbakkaloglu & Akin, 2012). AFRP offers superior confinement owing to its enhanced resistance compared to silicate substances, and its demand is expected to increase substantially in the future (Reglero Ruiz et al., 2017). The utilization of AFRP in the construction sector has markedly risen, with numerous studies undertaken about its applications (Djafar-Henni & Kassoul, 2018; Lobo et al., 2018; Silva, 2011; Y. Wang & Wu, 2010, 2011; H.-L. Wu et al., 2009), including an extensive investigation by Leung and Burgoyne on the confinement actions of concrete columns utilizing AFRP spirals (Leung & Burgoyne, 2001). Wu et al. developed a load-deformation model and chart for AFRP-confined circular concrete pillars based on empirical and statistical examination. Similarly, Wang and Wu proposed confinement approaches for AFRP-wrapped square pillars through a separate experimental investigation (Y. Wang & Wu, 2010). In 2009, the impact of creep on the pivotal performance of AFRP-limited cement-based composite pillars was investigated by Wang and Zhang, both with and without iron-strengthening materials (Y. Wang & Zhang, 2009). The majority of studies have concentrated on the impact of FRP encapsulation in unreinforced concrete elements; Silva further examined the influence of AFRP coating on circular and quadrilateral reinforced concrete columns regarding lateral pressure and fracture (Silva, 2011). Wang and Wu introduced a comprehensive stress method for short AFRP-limited cement-based composite pillars in their research, considering the dimension impact (Y. Wang & Wu, 2011). Utilizing 81 empirical datasets, Djafar-Henni and Kassoul introduced solution-oriented methodologies for round columns, emphasizing strength, strain, and load-deformation connections (Djafar-Henni & Kassoul, 2018). Silva Lobo et al. introduced a new load-deformation method that can be used for round and quadrilateral pillars (Lobo et al., 2018). Artificial Intelligence and machine

learning approaches have been increasingly developed in the field of Civil engineering applications (Afkhami Hoor & Esmaeili-Falak, 2024; Bagherabad et al., 2025; Esmaeili-Falak & Benemaran, 2024; Kou et al., 2024; Sun et al., 2024; Yaychi & Esmaeili-Falak, 2024). Recent investigations show that ML notably enhances forecasting precision for FRP-confined concrete acting, especially where regional models fall short. By incorporating agents like fiber orientation and substance attributes, ML approaches - particularly ensemble models - offer reliable forecasting of resistance and strain, boosting the design of FRP-strengthened structures (Gharaei-Moghaddam et al., 2023; Zarei et al., 2024), (L. Shang et al., 2025), (NadimiShahraki & Reisi, 2020), (Arabshahi et al., 2020). ML, especially reinforcement models, can predict the fire resistance of FRP-reinforced concrete beams with an accuracy of over 92%, replacing regional, costly methods (Kumarawadu et al., 2024).

Prior research demonstrates an increasing interest in the utilization of AFRP in structures; thus, this investigation offers special design links and uses machine learning approaches to forecast structural activity (Dawei et al., 2023; Ebrahim & Mahzad, 2024; Esmaeili-Falak et al., 2019; Esmaeili-Falak & Sarkhani Benemaran, 2024; Leung & Burgoyne, 2001; Li et al., 2023; Liang & Bayrami, 2023; Y. Wang & Wu, 2010; Y. Wang & Zhang, 2009; Zhang et al., 2024). These approaches have been employed primarily to assess the mechanical characteristics of concrete structures, with investigations on the influence of graphite particles, silica, and ceramic dust on compressive resistance. Ahmad et al. examined the compressive resistance of concrete activated with alkali and graphite particles utilizing procedure charts, AdaBoost, and packing reversal methods (Ahmad et al., 2022).

In their research, Ahmad et al. examined the compressive resistance of concrete incorporating graphite and alkaline substances utilizing AdaBoost, packing reverser, and procedure chart algorithms, with the packing reverser demonstrating superior predictive precision (Ahmad et al., 2022). In their work, Shang et al. (M. Shang et al., 2022) assessed the compressive and tensile strengths of recycled concrete utilizing charts of the procedure and the AdaBoost algorithm, achieving an R² of 0.95. Ahmad and Farooq similarly illustrated the efficacy of gene expression programming in predicting the resistance and high performance of reused concrete (Ahmad et al., 2021) (Abdel-Basset et al., 2024). Amin et al. examined the tensile strength of recycled concrete utilizing chart examination, RF, and ANNs, with the RF model illustrating superior performance (Amin et al., 2022).

The purpose of this work was to quantitatively analyze the ultimate strain (ε_{cu}) of AFRP-wrapped circular columns. Numerous ML solutions that employ tree-based approaches were created in order to achieve this aim. For the purpose of the computer study, a tree-based technique that is known as LSSVR approach was used. During the procedure of estimating, the following parameters were taken into consideration: f_{co}, L, f_f, t_f, E_f, and d. These materials are used in a wide range of structural engineering domains due to AFRP's exceptional mechanical properties. This goal was achieved by training and evaluating tree models for the purpose of predicting ε_{cu} from the dataset using a subset of the dataset that was published in the literature and had 156 samples. In order to get precise values for the decision variables, this work combined LSSVR analysis with a metaheuristic optimization method called the AHO and the GTO. Hence, it is of utmost importance to have estimation frameworks that are both dependable and precise for the ε_{cu} of circular AFRP-wrapped columns that are readily accessible.

2. Methods

This research uses a mix of machine learning algorithms and optimization strategies inspired by nature to provide a reliable prediction framework for determining the ε_cu of AFRP-confined concrete columns. This methodology's justification is to use the advantages of least square support vector regression (LSSVR) for regression tasks while optimizing its performance through efficient hyperparameter tuning with two sophisticated metaheuristic optimizers: the Giant Trevally Optimizer (GTO) and the Artificial Hummingbird Optimizer (AHO). Through model parameter optimization based on experimental data from literature, the suggested method seeks to increase prediction accuracy and generalizability.

2.1 Artificial Hummingbird Optimizer (AHO)

AHO is a numerical optimization based on the crowd that primarily emulates three distinct searching conducts exhibited by hummingbirds: conducted searching, regional searching, and translocate searching (Fig. 1). Three types of soaring proficiencies are simulated during the searching procedure: multi-directional, oblique, and length way soaring. Additionally, an access table is created to mimic the hummingbird's exceptional recollection capacity. This table serves as an attendant for the hummingbird to achieve universal development in the formula (Zhao et al., 2022). Three aerial abilities are described as the following:

The soaring proficiency simulation now includes the d-D area, with lengthways soaring being defined in the following manner (Zhao et al., 2022):

$$D^{(i)} = \begin{cases} 1 \ if \ i = randi([1,d]) \ i = 1, \dots, d \\ 0 \qquad\qquad else \end{cases} \quad (1)$$

An oblique soaring is characterized by the following (Zhao et al., 2022):

$$D^{(i)} = \begin{cases} 1 \ if \ i = p(j) \ P = randperm(k), k \in [2, \lceil r_1(d-2) \rceil + 1] \\ 0 \qquad\qquad else \end{cases} \quad (2)$$

Multi-directional soaring can be described as the ability to move in any direction (Zhao et al., 2022).

$$D^{(i)} = 1 \quad i = 1, \dots, d \quad (3)$$

In a $d - D$ area, an oblique soaring occurs within a hyper box, where $randi([1, d])$ produces an accidental integer among 1 and d, randperm(k) generates an accidental permutation of integers from 1 to k, and r_1 represents an accidental value between 0 and 1.

The AHO formula begins by initializing a collection of accidental solutions and a visiting table. During each repetition, there is a 1/2% chance of either conducted or regional searching being performed. Hummingbirds have the ability to travel toward their desired power supply resources by utilizing conducted research, which relies on nectar deposit prices and a consultable table. Through regional research, hummingbirds can efficiently explore neighboring areas within their land and discover potential fresh power supply resources. Travel searching occurs every other repetition. Throughout the process, all activities and computations are carried out bilaterally so long as the end regulation is met. Ultimately, the power supply resource that exhibits the highest precision of nectar-deposit renewal is selected and returned as an estimated universal superlative.

1. A group of n hummingbirds are accidentally assigned to n power supply resources in the following manner (Zhao et al., 2022):

$$x_i = Low + r \times (Up - Low) \quad i = 1, \dots, n \quad (4)$$

In a d-dimensional issue, the lowest and highest borders are denoted as Low and Up, in the same order. An accidental angle r is defined within the range [0, 1], while xi indicates the situation of the ith power supply resource (Rivandi & Jamili Oskouie, 2024; Zhao et al., 2022).

$$VT_{i,j} = \begin{cases} 0 \quad if \quad i \neq j \\ null \quad i = j \end{cases} \quad (5)$$

In the case where i is equal to j, the value of $VT_{i,j}$ being null signifies that a hummingbird is feeding at its designated power supply resource. On the other hand, if i is not equal to j and $VT_{i,j}$ is equal to 0, it indicates that the ith hummingbird has recently visited the jth power supply resource during the current repetition.

2. Conducted research: Utilizing its soaring capacities mentioned earlier, the hummingbird is able to reach its desired power supply resource and identify potential power supply resources. The arithmetical equation for simulating conducted search treatment and possible power supply resources is as shown (Zhao et al., 2022):

$$v_i(t + 1) = x_{i,tar}(t) + a \times D \times \left(x_i(t) - x_{i,tar}(t)\right) \quad (6)$$

$$a \sim N(0,1) \quad (7)$$

The situation of the ith hummingbird power supply resource at time t is denoted by x_i (t), while the location of the ith hummingbird aim power supply resource at time t is denoted by $x_{i,tar}$ (t). The variable a follows a normal distribution with an average of 0 and an excellence divergence of 1.

The ith power supply resource's location update is outlined below (Zhao et al., 2022):

$$x_i(t + 1) = \begin{cases} x_i(t) & f(x_i(t)) \leq f(v_i(t + 1)) \\ v_i(t + 1) & f(x_i(t)) > f(v_i(t + 1)) \end{cases} \quad (8)$$

The subordinate f (·) represents the fitness quantity. According to Eq. (8), if the nectar deposit amount of the applicant power supply resource surpasses that of the present one, the hummingbird will leave the present power supply resource and remain at the applicant resource determined by Eq. (6) for nutrition.

3. Regional searching: Once a hummingbird has consumed nectar to shape a particular power supply resource, it may explore other areas within its land to discover novel power supply that could potentially be more beneficial. The numerical equation used to simulate how hummingbirds conduct regional seeking when searching for a power supply in their lands is as shown below (Zhao et al., 2022):

$$v_i(t + 1) = x_i(t) + b \times D \times x_i(t) \quad (9)$$

$$b \sim N(0,1) \quad (10)$$

In cases where b follows a normal distribution with a mean of 0 and a standard deviation of 1, the data conforms to a standard normal model.

4. In regions where the power supply is regularly limited for hummingbirds, they will often travel to further situations in search of a power supply. The AHO formula includes a defined travel factor. When the value of repetitions surpasses the predefined quantity of the travel factor, the hummingbirds from the power supply resource with the lowest deposit amount will accidentally move to a fresh

power supply resource within the quest area. At this stage, the hummingbird will forsake its initial resource and remain at the novel resource for searching. Subsequently, the travel search of the hummingbird from the resource with the lowest nectar deposit amount to the accidentally generated novel resource can be described as below (Zhao et al., 2022):

$$x_{wor}(t + 1) = Low + r \times (Up - Low) \qquad (11)$$

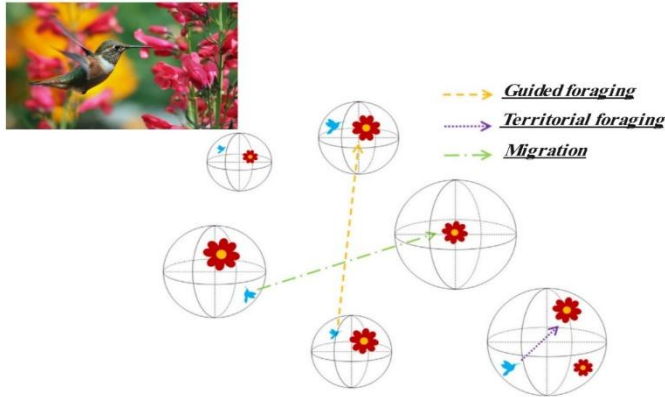In the crowd, x_{wor} represents the power supply resource that has the smallest amount of nectar deposit.

Fig. 1 3 foraging behaviors of AHO

2.2 Giant Trevally Optimizer (GTO)

The GTO formula, a novel probabilistic advanced search strategy improvement technique (Sadeeq & Abdulazeez, 2022), draws inspiration from the smart changing methods employed by huge trevallies. Initially, huge trevallies engage in a thorough exploration to meticulously choose their chasing grounds. Subsequently, the marine hunter commences its pursuit of the intended victim, ultimately leaping out of the water to execute a swift assault. The overall process of the huge trevallies' chasing methodology can be categorized into the subsequent stages:

Stage one: Comprehensive research (Discovery Stage)

The huge trevally's method of identifying power supply resources involves scanning the search zone, which is a process that is replicated in this stage. Eq. (12) is then utilized to simulate the search conduct of this marine hunter (Sadeeq & Abdulazeez, 2022).

$$X(t + 1) = Best_P \times R + ((Max - Min) \times R + Min) \times Levy(Dim) \quad (12)$$

The subsequent situation vector of the huge trevally, denoted as $X(t + 1)$, represents the coming revolution in the quest process. Based on the optimal position discovered in the previous search, the parameter $Best_P$ designates the present search area. The highest and lowest numbers of the issue at hand are referred to as maximum and minimum, in the same order. The parameter R assumes numbers within the interval of [0,1]. The term $Levy(Dim)$ denotes the Levy soaring.

Stage two: Selecting the region (Discovery Stage)

In this stage, the huge trevallies begin moving towards the victim region to locate their victim within the designated search area. The numerical representation for the updated condition of the prospect's huge trevally resolution at this stage can be expressed as (Sadeeq & Abdulazeez, 2022):

$$X(t + 1) = Best_P \times A \times R + Mean_{info} - X_i(t) \times R \qquad (13)$$

With a collection of 0.4, $X_i(t)$ denoting the present situation of the marine hunters and $Mean_{info}$ representing the average, it is evident that the huge trevallies have utilized all available primary data.

Stage three: Executing the Assault (Utilization Stage)

This stage of the formula involves the trevally starting to chase the bird. Once in proximity, the trevally executes a remarkable leap out of the water to assault its victim. In the context of the GTO formula, it is postulated that trevallies undergo visual distortion primarily due to the refraction of light as it passes through different media. This phenomenon is illustrated in Fig. 2, which demonstrates how light originating from dot A in the initial medium traverses the interface to enter the secondary medium, ultimately arriving at dot B. As a result, the visual perception of these predatory fish is likely influenced by this optical process, impacting their hunting strategies and overall behavior. In GTO, the bird assumes the role of the object, as illustrated in Fig. 2, while the giant trevally assumes the figure of the spectator. The visual distortion caused by light refraction is represented by the dotted line in Fig. 2, indicating that the bird appears to be positioned at a greater height than its actual elevation.

Hence, if the angle of incidence is given, the angle of defeat can be determined, and vice versa. The Snell's rule (Bennett, 2022) can be represented by the following equation (Sadeeq & Abdulazeez, 2022).

$$\eta_1 \sin\theta_1 = \eta_2 \sin\theta_2 \qquad (14)$$

In the given scenario, the quantities of $\eta_1 = 1.00029$ and $\eta_2 = 1.33$ correspond to the absolute defeat indices of air and water in the same order. On the other hand, θ_1 and θ_2 denote the angle of occurrence and angle of defeat in the same order. The angle θ_2 is an accidentally selected value within the range of [0,360]. According to Eq. (14), the angle θ_1 can be determined by utilizing the following formula (Sadeeq & Abdulazeez, 2022):

$$\sin\theta_1 = \frac{\eta_2}{\eta_1} \sin\theta_2 \qquad (15)$$

Next, the optical deformation V can be determined using Eq. (16) (Sadeeq & Abdulazeez, 2022).

$$V = \sin(\theta_1) \times D \qquad (16)$$

The space between the bird and the sea hunter is denoted by D. Eq. (17), which can be utilized for calculating this space (Sadeeq & Abdulazeez, 2022).

$$D = |(Best_P - X_i(t))| \qquad (17)$$

The improved resolution refers to the victim's location. By utilizing Eq. (18), a numerical representation of the behavior of giant trevally as they pursue prey and leap out of the water can be created (Sadeeq & Abdulazeez, 2022).

$$X(t + 1) = L + V + H \qquad (18)$$

L denotes the initiate speed necessary to replicate the act of capturing the victim and can be computed using Eq. (19) (Sadeeq & Abdulazeez, 2022).

$$L = X_i(t) \times \sin(\theta_2) \times F_{obj}(X_i(t)) \qquad (19)$$

$F_{obj}(X_i(t))$ represents the aim subordinate number. The improvement tool can dynamically facilitate a seamless shift from discovery to utilization stages, as denoted by the term H in Eq. (18). The number of H is calculated according to Eq. (20) (Sadeeq & Abdulazeez, 2022).

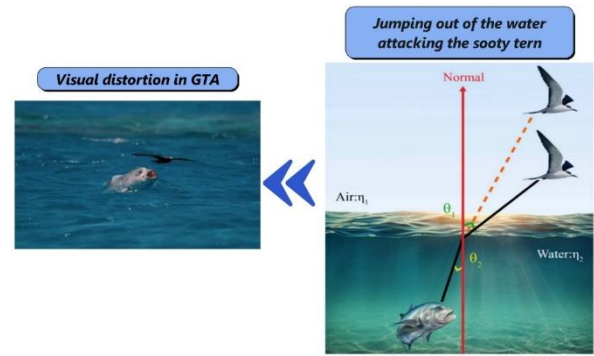$$H = R \times \left(2 - t \times \frac{2}{T}\right) \qquad (20)$$

Fig. 2 The attacking process of GTA

2.3 Description of Least Square Support Vector Regression (LSSVR)

LSSVR, an advanced ML technique, is an improved repetition of the SVR method, showcasing impressive abilities in modeling non-linear subordinates (Suykens & Vandewalle, 1999). Previous research has indicated that LSSVR exhibits strong learning potential, particularly in its application to address challenges within civil and ecological engineering domains (Bemani et al., 2020; Tian, 2020). This instructional approach utilizes a set of linear equations to educate the model in order to address the limitation of the second degree-constrained improvement program found in the SVM/SVR techniques. Consequently, LSSVR emerges as a low-variable method that is straightforward to implement mathematically. The improvement issue conceptualization associated with LSSVR can be expressed as below (Suykens & Vandewalle, 1999):

$$Minimize \frac{1}{2}\omega^T \omega + \frac{1}{2}\gamma \sum_{j=1}^{N}(e_j^2) \qquad (21)$$

The mass and bias vectors are represented by ω and b in the same order. The regularization agent γ is used to balance the amplification of the model while e_j represents the regression fault. The subordinate φ, which is defined in SVR, will be linearized. Hence, by utilizing the Lagrange subordinate and its derivative attributes, the system is transformed into a linear form, allowing it to be expressed concisely as (Suykens & Vandewalle, 1999):

$$\begin{bmatrix} 0 & 1_N^T \\ 1_N & \Omega + \gamma^{-1}1_N \end{bmatrix} \begin{bmatrix} b \\ \alpha \end{bmatrix} = \begin{bmatrix} 0 \\ Y \end{bmatrix} \qquad (22)$$

In the aforementioned context, the symbol 1_N represented the identity matrix with dimensions (N×N). The Lagrange multipliers are represented by $\alpha = [\alpha_1, \alpha_2, ..., \alpha_N]^T$, while the result vector is denoted as $Y = [y_1, y_2, ..., y_N]^T$. The kernel matrix Ω encompasses the kernel subordinate K. The efficiency of the RBF leads to its utilization in this study for modeling the kernel subordinate. Consequently, the solution of Eq. (22) can be expressed as the subsequent equation (Suykens & Vandewalle, 1999):

$$f(x) = \sum_{j=1}^{N} \alpha_j K(X_j, X_i) + b \qquad (23)$$

The LSSVR model's improved outcomes are significantly influenced by its hyper-variables (σ^2, γ).

Coupled and Tuned LSSVR

The objective of developing an LSSVR model is to create a robust and flexible ML technique that can perform classification and regression tasks with accuracy and dependability. The performance of LSSVR frameworks is strongly influenced by their hyperparameters, which may be changed using optimization approaches or trial-and-error. The study found that the following are the main LSSVR model hyperparameters that may be changed to optimize efficiency:

The regularization parameter (γ), also known as the cost parameter, manages the trade-off between minimizing model intricacy and obtaining a small error on the learning set. An increased value of γ indicates a closer match to the learning set, which might result in overfitting. A lower value of γ aims to simplify the model, which may aid in generalization but may cause the learning set to underfit.

The parameters of the kernel function specify how input data is converted into the feature area. The Radial Basis Function (RBF) Kernel was chosen for this investigation, with the kernel width (c) serving as its key variable. c regulates the kernel's spread and, hence, the impact of every learning sample.

An explanation of the procedures for adjusting the hyperparameters of an LSSVR model is provided below: a) The adjustable hyperparameters (c and γ) were identified. Research and data from the LSSVR library were used to determine each one's range. b) The dataset was divided between learning and testing sets in a 75/25 ratio. Following that, a tuning strategy utilizing optimization techniques was examined. The purpose of this effort was to fine-tune the hyperparameters by connecting LSSVR to two newly developed optimization techniques, AHO and GTO. d) The training dataset was then introduced to generate initialized models. Employing various hyperparameter mixtures, the search will train many models and assess each one's performance. e) Following the completion of the search, the results were analyzed to identify the ideal hyperparameters by using the RMSE values that were determined to be the aim function f) The effectiveness of the final model was evaluated on a different test set in order to ascertain its performance on unseen data. Table 1 provides the first and optimized values of associated variables for connected models and optimization techniques.

Table 1. Parameters values

AHO		GTO		
Parameters	Value	Parameters		Value
Iterative cycles number	200	Iterative cycles number		200
Proposed solutions	20	Proposed solutions		10
Independent runs number	5	Independent runs number		5
Coefficient of migration	$2n$	A		0.4
Specific index	Value	Specific index		Value
$LSSVR(A)$ c	1.53	$LSSVR(G)$	c	1.02
γ	25		γ	31
Function	RBF		Function	RBF

2.4 Collected Data Processing

The application of concrete enclosures with reinforced agent-enhanced macromolecule (FRP) is a prevalent method for stabilizing structures (See Fig. 3). This research utilizes tree-based (DT) approaches to evaluate the effectiveness and precision of the Beka method in estimating the ultimate strain variable (ε_{cu}) of pillars enclosed in AFRP. It is important to highlight that utilizing meta-parameters for forecasting can significantly improve the accuracy of results. Some of these methods involve the AHO, GTO, and LSSVR. The precise and strategic choice of input

variables for initiating forecasting procedures stands as a critical element in attaining precise outcomes and simulations with exceptional precision. Based on the dependable sources found in the technical literature (Cakiroglu, 2023; Cheek et al., 2011; Dai et al., 2011; Lim & Ozbakkaloglu, 2015; Muzata et al., 2024; Nanni & Bradford, 1995; Ozbakkaloglu, 2013; Ozbakkaloglu & Vincent, 2014; Rochette & Labossiere, 2000; Suter & Pinzelli, 2001; Toutanji & Deng, 2002; Vincent & Ozbakkaloglu, 2013; Watanabe et al., 1997; G. Wu et al., 2008; Yin, 2025), a sum of 156 accurate data points was gathered. Subsequently, the collected data was segregated into input and outcome categories and further divided into training and testing sets, with 75% and 25% allocation in the same order based on the total data volume (Aghayari Hir et al., 2023; Benemaran, 2023). Furthermore, cross-validation methods were used throughout the model generation stage to guarantee the robustness and generalizability of the findings. This method facilitated a more dependable evaluation of model performance and reduced the likelihood of overfitting or data-specific abnormalities affecting the assessment. The integration of randomization, cross-validation, and a representative train-test division enhances the validity of the modeling framework used in this study. Specimen span in mm (d), modulus of elasticity in GPa (E_f), pillar height in mm (L), ultimate tensile strength in MPa (f_f), total width cover in mm (t_f), unconstrained compressive strength in MPa (f_{co}), and the variable outcome parameter, ultimate strain (ε_{cu}), are among the parameters that are provided. Upon partitioning the variables at hand, the subsequent stage involves examining and verifying the distribution of data and their interrelationships using statistical metrics as outlined in Table 2. This table incorporates 7 assessment criteria aligned with this objective, encompassing minimum, maximum, standard deviation, kurtosis, range, mean, and median.

The standard deviation is a measure of dispersion that indicates the average distance of the data from the mean value. Kurtosis quantifies the extent to which the tails of a distribution deviate from the center of the distribution curve (mean). The domain index generates an array comprising a range of elements. In the realm of statistics and probability theory, the median serves as one of the indicators of central tendency. The median divides a statistical population or probability distribution into two equal parts, distinguishing it from the mean by its resistance to extreme values. The concepts of minimum, maximum, and mean are also commonly utilized. It is important to mention that in this table, each indicator has been applied individually to the training and testing sections in order to conduct the investigations with greater precision.
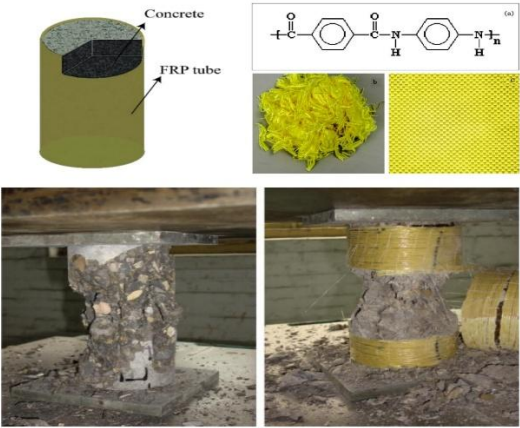

Fig. 3 A visual of the real structural application of the developed model (Yang et al., 2015)

Table 2. The characteristics of dependent and independent variables in non-normalized form

Category	Index	Input variables						Target variable
		f_{co}	d	L	f_f	E_f	t_f	ε_{cu}
		MPa	mm	mm	MPa	GPa	mm	%
Training phase	Minimum	28.79	70	152	2060	99	0.057	0.37
	Maximum	119.3	194	762	3732	128.5	1.2	4.78
	Standard deviation	28.773	29.422	162.264	447.144	8.606	0.259	1.017
	Kurtosis	-1.4168	-1.0509	2.5411	0.3468	0.6353	0.2157	-0.3940
	Range	90.51	124	610	1672	29.5	1.143	4.41
	Average	74.259	130.744	323.462	2653.821	118.820	0.551	1.978
	Median	78.5	152	305	2663	118	0.6	1.78
Testing phase	Minimum	28.79	70	152	2060	99	0.057	0.36
	Maximum	119.3	194	762	2930	128.5	1.2	3.55
	Standard deviation	31.920	29.809	117.885	332.248	8.998	0.312	0.878
	Kurtosis	-1.5550	-1.1449	5.9119	-1.4159	1.0152	-0.2563	-0.5317
	Range	90.51	124	610	870	29.5	1.143	3.19
	Average	67.966	126.410	290.436	2549.769	119.523	0.557	1.896
	Median	57.5	150	305	2663	120	0.6	1.88

Data normalization, also known as data de-scaling, is a method for standardizing the range of values connected to different study variables. Data can be equally scaled using normalization techniques when the variables under study have diverse units of measurement. Normalization is a fundamental concept in multi-criteria decision-making techniques like AHP and ANP. It allows for the comparison of data with varying measurement criteria by de-scaling in these methods. Normalization, also referred to as standardization, is a widely employed technique in the examination of ANN and data envelopment analysis. To achieve standardization of an element, it is necessary to subtract said element from the mean and then divide it by the standard deviation. Conversely, in order to normalize an element, the approach involves minimizing the element and dividing it by the range of changes. The data normalization method employed in this article is utilized to simulate the forecasted data.

Visual aids in the form of diagrams have been employed to gain a deeper insight and enhance comprehension of the prediction derived from AI methods for closer examination. Data visualization enables users to comprehend data effortlessly by presenting trends, patterns, and graphs in a visually appealing manner. It facilitates the swift and efficient interpretation of vast quantities of data. To effectively convey insights and discoveries to individuals without expertise in the field, it is crucial to make data easily understandable and applicable. By utilizing data visualization techniques, the value and potential risks associated with various opportunities and strategies can be assessed, enabling the determination of which ones are worth pursuing. This categorization and identification process aids in making informed decisions. This article utilizes pie charts to visually represent the data and illustrate the characteristics of the desired information, as shown in Fig. 4.

Pie charts, alternatively referred to as polar or radar charts, are visual depictions of multivariate data. In these charts, variables are depicted as points or vectors along radial axes, with each axis representing a distinct variable. A radial grid is formed by these axes that stem from a central point and spread outwards, evenly spaced around a circle. Pie charts prove to be highly effective in visualizing and comparing data sets with multiple variables, allowing for the identification of patterns and relationships that may not be easily discernible in other forms of visualization. The semicircle diagram is utilized to examine seven variables, consisting of 6 inputs and one output, in various intervals. This analysis helps identify clusters, outliers, and correlations between variables. For instance, the variable (E_f) within the range of 0 to 1 demonstrates a significant correlation within the data.
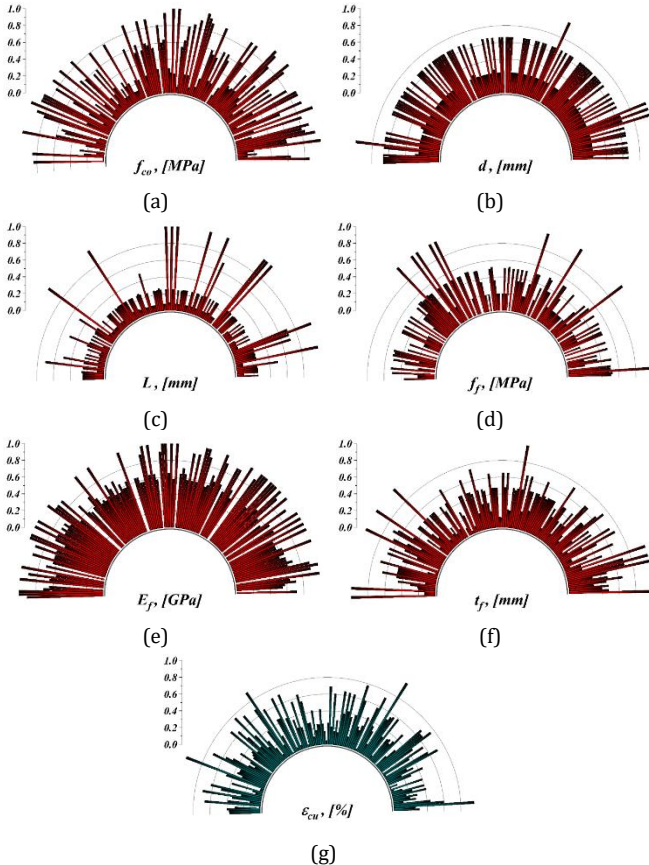

Fig. 4 The distribution of attributes in normalized form

The graph displayed in Fig. 5 illustrates the features of the normalized data referred to as the Spearman graph. A Spearman plot, alternatively referred to as a Spearman rank correlation plot or a Spearman row plot, serves as a visual tool to depict the association between 2 variables in relation to their rank order. It relies on Spearman's rank correlation coefficient (ρ), which quantifies the magnitude and direction of the univariate relationship between the two parameters.

The main characteristics of the Spearman design include:
Scatter plot: A Spearman plot is essentially a scatter plot that exhibits the ordered values of 2 variables as data points.
Rank order: The x-axis and y-axis represent the relative positions of 2 variables rather than their specific values.
Monotonic relationship: The chart aids in illustrating the level of monotonicity between variables, indicating that when one variable rises, the other variable typically rises (positive correlation) or falls (negative correlation).
Correlation Coefficient (ρ): Spearman's rank correlation coefficient (ρ) is derived from ranked data and varies between -1 (indicating a perfect negative correlation) and 1 (indicating a perfect positive correlation). A quantity of 0 signifies the absence of correlation.

Spearman's correlation differs from Pearson's correlation in that it examines the association between parameter rankings, whereas Pearson's correlation assesses the linear connection between observed quantities. Spearman plots are especially advantageous for analyzing ordinal or non-normally distributed data, offering valuable insights into the univariate relationships between variables in diverse areas of study. Upon scrutiny of the illustration, it is apparent that f_{co} and t_f variables are positively correlated with a value of 0.71, indicating a strong relationship. Subsequently, f_f and ε_{cu} variables are ranked second in terms of positive correlation, with a value of 0.66. Conversely, L and f_f variables exhibit the highest negative correlation at -0.29. In general, the data exhibits a notable level of interdependence, as reflected by their positions on the chart.
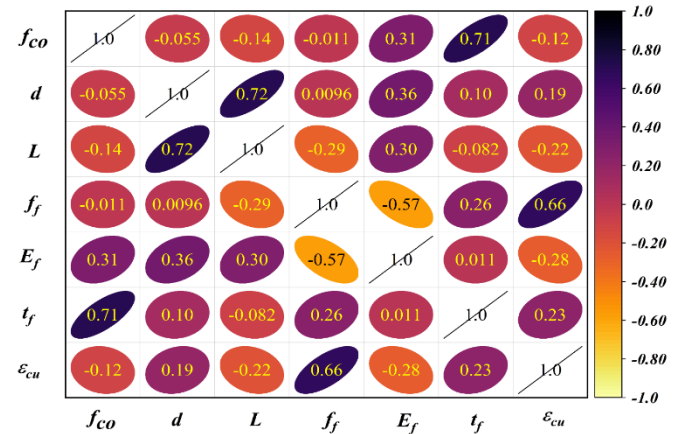

Fig. 5. The Spearman correlation values

2.5   Performance Criteria

A variety of indicators were taken into account and computed to assess the effectiveness of the successfully constructed LSSVR frameworks. In order to facilitate the execution of this research, the following is a synopsis of the indicators that were utilized:
Coefficient of determination:

$$R^2 = \left(\frac{\sum_{i=1}^{m}(Z_i - \bar{Z})(C_i - \bar{C})}{\sqrt{[\sum_{i=1}^{m}(Z_i - Z)^2][\sum_{i=1}^{m}(C_i - \bar{C})^2]}} \right) \qquad (24)$$

Root mean square error:

$$RMSE = \sqrt{\frac{1}{m}\sum_{i=1}^{m}(C_i - Z_i)^2} \qquad (25)$$

Mean absolute error:

$$MAE = \frac{1}{m}\sum_{i=1}^{m}|C_i - Z_i| \qquad (26)$$

Adjusted Coefficient of determination:

$$Adj\_R^2 = 1 - \frac{(1-R^2)\times(m-1)}{m-k-1} \qquad (27)$$

Mean Squared Percentage Error:

$$MSPE = \frac{1}{m}\sum_{i=2}^{m}\left(\frac{Z_i-C_i}{Z_i}\times 100\right)^2 \qquad (28)$$

Theil inequality coefficient:

$$TIC = \frac{\sqrt{\frac{1}{m}\sum_{i=1}^{m}(C_i-Z_i)^2}}{\left(\sqrt{\frac{1}{m}\sum_{i=1}^{m}C_i{}^2} + \sqrt{\frac{1}{m}\sum_{i=1}^{m}Z_i{}^2}\right)} \qquad (29)$$

Uncertainty analysis with a 95% confidence level:
$$U_{95} = 1.96\sqrt{(SD^2 + RMSE^2)} \qquad (30)$$

The following parameters can be interpreted using the provided equations: Z_i denotes the measured ε_{cu}, $\bar{Z}$ shows the mean of the measured ε_{cu}, C_i represents the predicted value of ε_{cu}, $\bar{C}$ stands for the mean of the predicted value of ε_{cu}, n is the total number of observations, and k is the number of predictors (excluding the intercept) in the model.

3. Results and Discussion

Table 3. The workability of the created regression analysis

Phase	Metrics	Best Value	Single regressions	Created hybrid regressions		Variance
			LSSVR	LSSVR(A)	LSSVR(G)	%
Training phase	R^2	The higher, the best	0.9381	0.9862	0.9882	0.202799
Testing phase			0.9113	0.9894	0.9911	0.171821
Training phase	RMSE	The lower, the best	0.354	0.1196	0.1105	-7.6087
Testing phase			0.268	0.0912	0.0828	-9.21053
Training phase	MAE	The lower, the best		0.0676	0.0591	-12.574
Testing phase				0.0559	0.0434	-22.3614
Training phase	Adj_R^2	The higher, the best		0.9861	0.9881	0.202819
Testing phase				0.9889	0.9909	0.202245
Training phase	MSPE	The lower, the best		29.6534	19.4473	-34.418
Testing phase				21.9875	14.1405	-35.6885
Training phase	TIC	The lower, the best		0.0269	0.0249	-7.43494
Testing phase				0.0218	0.0198	-9.17431
Training phase	$U_{95\%}$	The lower, the best		0.3321	0.3068	-7.61819
Testing phase				0.2543	0.2308	-9.24105

The AHO and GTO techniques, also known as LSSVR(A) and LSSVR(G), were integrated with the LSSVR methodologies to calculate the ε_{cu} of AFRP. This made it possible to compute the AFRP. According to the metrics R^2, RMSE, MAE, Adj_R^2, MSPE, TIC, and U95, both LSSVR(A) and LSSVR(G) were tested for their accuracy in forecasting ε_{cu} (Table 3). Prior to the development of the product, several assessments were carried out. During the evaluation and learning stages, the ε_{cu} values that were observed and predicted for the LSSVR(A) and LSSVR(G) approaches are shown in Fig. 6. Several measurements were taken of these parameters on several occasions. In addition, the image illustrates the error percentage of the predicted and observed ε_{cu} for each individual participant throughout the length of the experiment.

When it comes to calculating the ε_{cu} of AFRP, it is obvious that the LSSVR(A) and LSSVR(G) approaches offer a great degree of potential. This notion is supported by the data. In the course of the training and assessment stages, it was demonstrated that the LSSVR(A) approach attained R^2 values of 0.9862 and 0.9894, respectively. This indicates that the process had an exceptional degree of dependability. In regard to R^2 values, the LSSVR(G) technique fared much superior to the LSSVR(A) method. For the learning and assessment phases, the corresponding values were 0.9882 and 0.9911, respectively. The most precise model was represented by Adj_R^2, which was one of the estimated metrics that showed a similar trend in performance. Other metrics demonstrated a trend that was equivalent to the one shown by Adj_R^2. It is possible that the reliability of the method might be improved by including an additional assessment of indicators that depend on mistakes. This is really something that can be accomplished. This being said, in order to accomplish this specific goal, it is crucial to carry out a thorough analysis of the efficacy of several other measures, such as RMSE, MAE, MSPE, TIC, and U95. Based on these indications, the lower one denotes a more reliable accuracy than the higher one. According to a review of the values generated for these variables, the LSSVR(G) model was able to acquire the lowest quantities while maintaining the highest level of accuracy, which set it apart from the other models. Following the examination of the values generated for these variables, this became apparent. The LSSVR(G) obtained the lowest RMSE index values during the training and evaluation phases, with respective values of 0.1105 and 0.0828. LSSVR(A), on the other hand, achieved values that were greater than these during the learning and evaluation phases, respectively, of 0.1196 and 0.0912. Regarding MAE index values, throughout the training and assessment stages, the LSSVR(A) achieved values of 0.0676 and 0.0559, respectively, while the LSSVR(G) received the smallest values of 0.0591 and 0.0434. The two models that were developed for these metrics have a variation percentage of at least 7%; in some cases, this variance is lowered by 36%, indicating the LSSVR(G)'s capability and reliability for forecasting purposes.

The 95% confidence interval (U95), which is used in this study to assess uncertainty, indicates that the actual value is probably going to fall somewhere within this range surrounding the observed or anticipated value. By taking into account both the measurement variability and the prediction quality, U95 offers a reliable assessment of the overall uncertainty. This helps the procedure of making well-informed decisions by illuminating the reliability of the measurements. Throughout the training and assessment stages, the LSSVR(G) had the lowest values, with U95 index values of 0.3068 and 0.2308, respectively. However, these values fell short of the 0.3321 and 0.2543 values that LSSVR(A) achieved throughout the learning and assessment stages. Although both models are reliable and accurate, the reasoning and assessment indicators suggest that LSSVR(G) has a little advantage over the other.
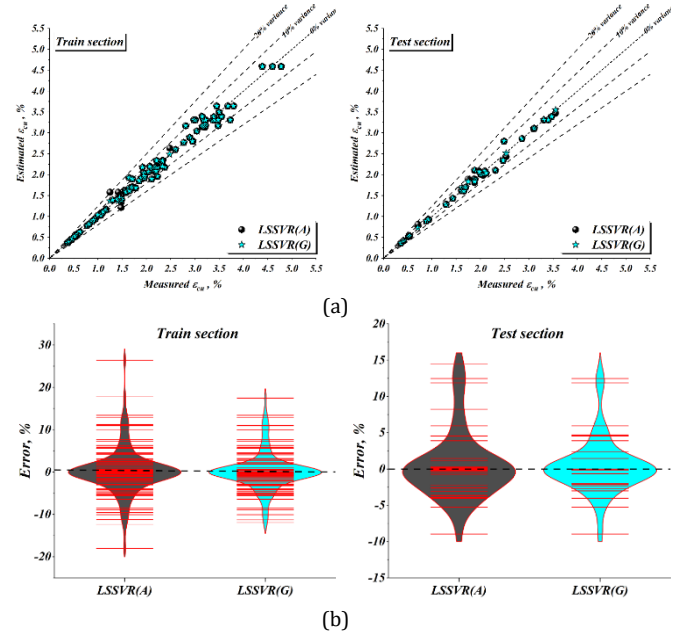

(a)

(b)

Fig. 6 The workability of the created regression analysis

To evaluate the impact of the input variables on the goal parameter, a feature significance analysis (F$_s$) was carried out on large datasets. The F$_s$ for a given input parameter (z) may be calculated utilizing the formula as follows:

$$F_s = \frac{\sum_{i=1}^{P} z_i t_i}{\sqrt{\sum_{i=1}^{P} z_i^2 \sum_{i=1}^{P} t_i^2}} \qquad (31)$$

The expected objective is represented by the parameter t_i, while the total number of data points is represented by the parameter P. The numerical value of P is 156 in this instance. The degree of correlation between every input and the anticipated aim is indicated by the F$_s$ number, which goes from 0 to 1. The high value of F_s, that is near 1, indicates the variable which has the most influence on prediction. Fig. 7 shows that the f_f at 0.9349 and d at 0.8929 have the greatest effect on the forecast of ε_{cu}. After that, the remaining input parameters were ranked from 3 to 6, with E_f, t_f, f_{co}, and L accounting for 0.8847, 0.8449, 0.809, and 0.7431, correspondingly. Since the dataset was created using empirical efforts, it is natural that every parameter has a noteworthy influence on the objective, yet eliminating any of them was not recommended.
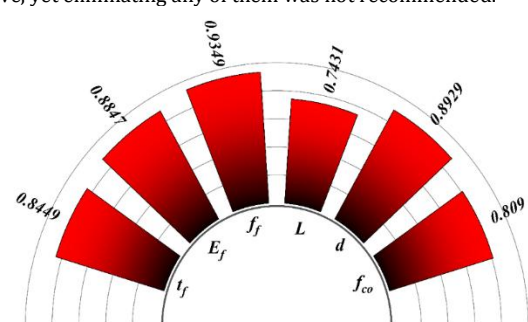

Fig. 7 Parameter importance analysis

A Taylor diagram is a valuable visual representation that allows researchers to evaluate and compare the effectiveness of various models or simulations against real-world observed data. This tool uses three crucial statistical measures: the correlation coefficient, standard deviation, and root mean square error. In the picture, the standard deviation measure of how much the model's predictions differ from the actual data is shown by the distance from the center point. A value close to 1 suggests a strong correspondence between the predictions and what is observed in reality. Additionally, the angle formed by each plotted point relative to the horizontal axis reveals the correlation between the model and the observed data. Contours radiating from the center illustrate models with lower error rates, while points located nearer to the observation point typically along the x-axis indicate higher error levels. This diagram effectively merges these statistical measures into a single visual, simplifying the comparison of model accuracy, variability, and correlation. For instance, as shown in Fig. 8, the performance of the developed models during both the training and testing phases is depicted. A model's closeness to the reference point signifies its accuracy and reliability. Interestingly, in both the training and testing phases, although the LSSVR(A) presented the acceptable accuracy, the model labeled LSSVR(G) is found closer to the reference point compared to LSSVR(A), depicting the roughly better performance. This observation underscores the complexity of model evaluation, where proximity to the reference point does not always equate to superior accuracy.
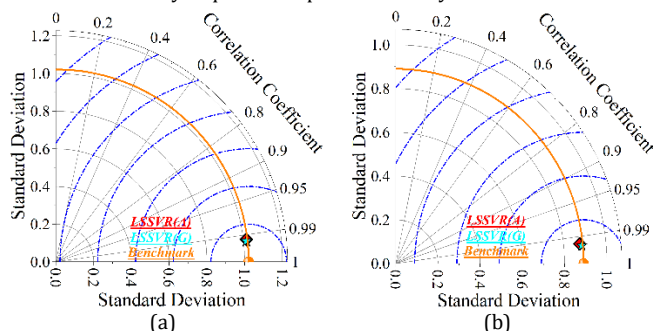

Fig. 8 The performance evaluation considering Taylor diagram analysis

4. Conclusion

The aim of this work was to quantitatively analyze the ultimate strain (ε_{cu}) of circular columns that were reinforced using AFRP. To accomplish this goal, several unique ML algorithms that employ tree-based techniques were developed. These two methods, known as LSSVR analysis and based on trees, were developed on a computer with the goal of doing this. The hyperparameters of this simulation have a significant impact on its correctness. The AHO and GTO techniques are used with LSSVR to determine the ideal combination of hyperparameters. Additionally, the unique sensitivity analysis approach is used to evaluate each parameter's impact on the target parameter.

The study's feature significance analysis reveals f_f at 0.9349 and d at 0.8929 had the biggest impact on ε_{cu} prediction. The other input variables were rated from 3 to 6, with E_f, t_f, f_{co}, and L at 0.8847, 0.8449, 0.809, and 0.7431. Since the dataset was constructed empirically, each variable has a significant impact on the target; however, deleting any was not advised.

The LSSVR(A) technique achieved R^2 values of 0.9862 and 0.9894 during training and evaluation. This shows high process reliability. The LSSVR(G) methodology exceeded the LSSVR(A) method in R^2 values. The learn and evaluation phases had 0.9882 and 0.9911 scores. Adj_R^2 indicated the best accurate model, with a comparable performance trend.

The LSSVR(G) has the lowest RMSE index values (0.1105 and 0.0828) during training and evaluation. In comparison, LSSVR(A) reached higher values of 0.1196 and 0.0912 during learning and evaluation. During training and assessment, the MAE index values for the LSSVR(A) were 0.0676 and 0.0559, while the MAE index values for the LSSVR(G) were the lowest at 0.0591 and 0.0434.

The forecasting competence and reliability of the LSSVR(G) are demonstrated by the variance percentages of the two models that were developed for these measures, which are at least 7%; in certain cases, this variance is reduced by 36%.

The LSSVR(G) had the lowest uncertainty values throughout training and assessment, 0.3068 and 0.2308, respectively. These values were lower than LSSVR(A)'s 0.3321 and 0.2543 learning and assessment values, thereby enhancing the precision, accuracy, comparability, and credibility of measurements.

The Taylor diagram effectively illustrates the performance of various models by integrating key statistical metrics, enabling a clear comparison of accuracy and variability. Notably, while LSSVR(G) is closer to the

reference point, LSSVR(A) still exhibits higher accuracy, highlighting the complexities of model evaluation.

References

Abdel-Basset, M., Mohamed, R., Hezam, I. M., Sallam, K. M., & Hameed, I. A. (2024). An Efficient Binary Hybrid Equilibrium Algorithm for Binary Optimization Problems: Analysis, Validation, and Case Studies. International Journal of Computational Intelligence Systems, 17(1), 98. https://doi.org/10.1007/s44196-024-00458-z

Afkhami Hoor, S., & Esmaeili-Falak, M. (2024). Innovative Approaches for Mitigating Soil Liquefaction: A State-of-the-Art Review of Techniques and Bibliometric Analysis. Indian Geotechnical Journal. https://doi.org/10.1007/s40098-024-01120-3

Aghayari Hir, M., Zaheri, M., & Rahimzadeh, N. (2023). Prediction of rural travel demand by spatial regression and artificial neural network methods (Tabriz County). Journal of Transportation Research (Tehran), 20(4), 367-386.

Ahmad, A., Ahmad, W., Aslam, F., & Joyklad, P. (2022). Compressive strength prediction of fly ash-based geopolymer concrete via advanced machine learning techniques. Case Studies in Construction Materials, 16, e00840. https://doi.org/10.1016/j.cscm.2021.e00840

hmad, A., Chaiyasarn, K., Farooq, F., Ahmad, W., Suparp, S., & Aslam, F. (2021). Compressive strength prediction via gene expression programming (GEP) and artificial neural network (ANN) for concrete containing RCA. Buildings, 11(8), 324. https://doi.org/10.3390/buildings11080324

Amin, M. N., Ahmad, A., Khan, K., Ahmad, W., Nazar, S., Faraz, M. I., & Alabdullah, A. A. (2022). Split tensile strength prediction of recycled aggregate-based sustainable concrete using artificial intelligence methods. Materials, 15(12), 4296. https://doi.org/10.3390/ma15124296

Arabshahi, A., Gharaei Moghaddam, N., & Tavakkolizadeh, M. (2015). Proposed slenderness limit for FRP circular concrete column. Third Conference on Smart Monitoring, Assessment and Rehabilitation of Civil Structures, Antalya, Turkey.

Arabshahi, A., Gharaei-Moghaddam, N., & Tavakkolizadeh, M. (2020). Development of applicable design models for concrete columns confined with aramid fiber reinforced polymer using Multi-Expression Programming. Structures, 23, 225-244. https://doi.org/10.1016/j.istruc.2019.09.019

Babak, A., Shayan, R., P, S. M., Navid, C., S, F. A., & Mazdak, T. (2024). Cold-Formed Cross-Sectional Folds with Optimal Signature Curve. Journal of Engineering Mechanics, 150(8), 04024045. https://doi.org/10.1061/JENMDT.EMENG-7708

Bagherabad, M. B., Rivandi, E., & Mehr, M. J. (2025). Machine Learning for Analyzing Effects of Various Factors on Business Economic. Authorea Preprints. https://doi.org/10.36227/techrxiv.174429010.09842200/v1

Bemani, A., Xiong, Q., Baghban, A., Habibzadeh, S., Mohammadi, A. H., & Doranehgard, M. H. (2020). Modeling of cetane number of biodiesels from fatty acid methyl ester (FAME) information using GA-, PSO-, and HGAPSO-LSSVM models. Renewable Energy, 150, 924-934. https://doi.org/10.1016/j.renene.2019.12.086

Benemaran, R. S. (2023). Application of extreme gradient boosting method for evaluating the properties of episodic failure of borehole breakout. Geoenergy Science and Engineering, 226, 211837. https://doi.org/10.1016/j.geoen.2023.211837

Bennett, C. A. (2022). Principles of physical optics. John Wiley & Sons.

Cakiroglu, C. (2023). Explainable data-driven ensemble learning models for the mechanical properties prediction of concrete confined by aramid fiber-reinforced polymer wraps using generative adversarial networks. Applied Sciences, 13(21), 11991. https://doi.org/10.3390/app132111991

Chastre, C., & Silva, M. A. G. (2010). Monotonic axial behavior and modelling of RC circular columns confined with CFRP. Engineering Structures, 32(8), 2268-2277. https://doi.org/10.1016/j.engstruct.2010.04.001

Cheek, J., Formichella, N., Graetz, D., & Varasteh, S. (2011). The behavior of ultra-high strength concrete in FRP confined concrete systems under axial compression. Honours Bachelor's Thesis, School of Civil, Environmental and Mining Engineering, Univ. of Adelaide, Adelaide, Australia.

Dai, J.-G., Bai, Y.-L., & Teng, J. G. (2011). Behavior and modeling of concrete confined with FRP composites of large deformability. Journal of Composites for Construction, 15(6), 963-973. https://doi.org/10.1061/(ASCE)CC.1943-5614.0000230

Dawei, Y., Bing, Z., Bingbing, G., Xibo, G., & Razzaghzadeh, B. (2023). Predicting the CPT-based pile set-up parameters using HHO-RF and PSO-RF hybrid models. Structural Engineering and Mechanics, An Int'l Journal, 86(5), 673-686.

Djafar-Henni, I., & Kassoul, A. (2018). Stress-strain model of confined concrete with Aramid FRP wraps. Construction and Building Materials, 186, 1016-1030. https://doi.org/10.1016/j.conbuildmat.2018.08.013

Ebrahim, H., & Mahzad, E.-F. (2024). Soil-Structure Interaction for Buried Conduits Influenced by the Coupled Effect of the Protective Layer and Trench Installation. Journal of Pipeline Systems Engineering and Practice, 15(2), 04024012. https://doi.org/10.1061/JPSEA2.PSENG-1547 https://doi.org/10.1061/JPSEA2.PSENG-1547

Elsanadedy, H. M., Al-Salloum, Y. A., Alsayed, S. H., & Iqbal, R. A. (2012). Experimental and numerical investigation of size effects in FRP-wrapped concrete columns. Construction and Building Materials, 29, 56-72. https://doi.org/10.1016/j.conbuildmat.2011.10.025

Esmaeili-Falak, M., & Benemaran, R. S. (2024). Ensemble Extreme Gradient Boosting based models to predict the bearing capacity of micropile group. Applied Ocean Research, 151, 104149. https://doi.org/https://doi.org/10.1016/j.apor.2024.104149

Esmaeili-Falak, M., Katebi, H., Vadiati, M., & Adamowski, J. (2019). Predicting triaxial compressive strength and Young's modulus of frozen sand using artificial intelligence methods. Journal of Cold Regions Engineering, 33(3), 04019007. https://doi.org/10.1061/(ASCE)CR.1943-5495.0000188

Esmaeili-Falak, M., & Sarkhani Benemaran, R. (2024). Application of optimization-based regression analysis for evaluation of frost durability of recycled aggregate concrete. Structural Concrete, 25(1), 716-737. https://doi.org/10.1002/suco.202300566

Fardis, M. N., & Khalili, H. H. (1982). FRP-encased concrete as a structural material. Magazine of Concrete Research, 34(121), 191-202. https://doi.org/10.1680/macr.1982.34.121.191

Faustino, P., Chastre, C., & Paula, R. (2014). Design model for square RC columns under compression confined with CFRP. Composites Part B: Engineering, 57, 187-198. https://doi.org/10.1016/j.compositesb.2013.09.052

Gharaei-Moghaddam, N., Arabshahi, A., & Tavakkolizadeh, M. (2023). Predictive models for the peak stress and ultimate strain of FRP confined concrete cylinders with inclined fiber orientations. Results in Engineering, 18, 101044. https://doi.org/10.1016/j.rineng.2023.101044

Hadi, M. N. S., Khan, Q. S., & Sheikh, M. N. (2016). Axial and flexural behavior of unreinforced and FRP bar reinforced circular concrete filled FRP tube columns. Construction and Building Materials, 122, 43-53. https://doi.org/10.1016/j.conbuildmat.2016.06.044

Jiang, T., & Teng, J. G. (2007). Analysis-oriented stress-strain models for FRP-confined concrete. Engineering Structures, 29(11), 2968-2986. https://doi.org/10.1016/j.engstruct.2007.01.010

Jiang, T., & Teng, J. G. (2012). Theoretical model for slender FRP-confined circular RC columns. Construction and Building Materials, 32, 66-76. https://doi.org/10.1016/j.conbuildmat.2010.11.109

Khorasani, A. M. M., Esfahani, M. R., & Sabzi, J. (2019). The effect of transverse and flexural reinforcement on deflection and cracking of GFRP bar reinforced concrete beams. Composites Part B: Engineering, 161, 530-546. https://doi.org/10.1016/j.compositesb.2018.12.127

Kou, H., Quan, J., Guo, S., & Hassankhani, E. (2024). Light and normal weight concretes shear strength estimation using tree-based tunned frameworks. Construction and Building Materials, 452, 138955. https://doi.org/https://doi.org/10.1016/j.conbuildmat.2024.138955

Kumarawadu, H., Weerasinghe, P., & Perera, J. S. (2024). Evaluating the Performance of Ensemble Machine Learning Algorithms over Traditional Machine Learning Algorithms for Predicting Fire Resistance in FRP Strengthened Concrete Beams. Electronic Journal of Structural Engineering, 24(3), 47-53. https://doi.org/10.56748/ejse.24661

Lam, L., & Teng, J. G. (2003). Design-oriented stress-strain model for FRP-confined concrete. Construction and Building Materials, 17(6-7), 471-489. https://doi.org/10.1016/S0950-0618(03)00045-X

Leung, H. Y., & Burgoyne, C. J. (2001). Compressive behavior of concrete confined by aramid fibre spirals. In Structural Engineering, Mechanics and Computation (pp. 1357-1364). Elsevier. https://doi.org/10.1016/B978-008043948-8/50151-X

Li, D., Zhang, X., Kang, Q., & Tavakkol, E. (2023). Estimation of unconfined compressive strength of marine clay modified with recycled tiles using hybridized extreme gradient boosting method. Construction and Building Materials, 393, 131992. https://doi.org/10.1016/j.conbuildmat.2023.131992

Liang, R., & Bayrami, B. (2023). Estimation of frost durability of recycled aggregate concrete by hybridized Random Forests algorithms. Steel and Composite Structures, 49(1), 91-107.

Lim, J. C., & Ozbakkaloglu, T. (2015). Hoop strains in FRP-confined concrete columns: experimental observations. Materials and Structures, 48, 2839-2854. https://doi.org/10.1617/s11527-014-0358-8

Lobo, P. S., Faustino, P., Jesus, M., & Marreiros, R. (2018). Design model of concrete for circular columns confined with AFRP. Composite Structures, 200, 69-78. https://doi.org/10.1016/j.compstruct.2018.05.094

Muzata, T. S., Matuana, L. M., & Rabnawaz, M. (2024). Challenges in the mechanical recycling and upcycling of mixed postconsumer recovered plastics (PCR): A review. Current Research in Green and Sustainable Chemistry, 100407. https://doi.org/10.1016/j.crgsc.2024.100407

NadimiShahraki, K., & Reisi, M. (2020). Stress-strain based method for analysis and design of FRP wrapped reinforced concrete columns. Structures, 28, 1818-1830. https://doi.org/10.1016/j.istruc.2020.10.002

Nanni, A., & Bradford, N. M. (1995). FRP jacketed concrete under uniaxial compression. Construction and Building Materials, 9(2), 115-124. https://doi.org/10.1016/0950-0618(95)00004-Y

Nguyen, H. D., Choi, E., & Park, K. (2018). Dilation behavior of normal strength concrete confined by FRP wire jackets. Construction and Building Materials, 190, 728-739. https://doi.org/10.1016/j.conbuildmat.2018.09.081

Ozbakkaloglu, T. (2013). Compressive behavior of concrete-filled FRP tube columns: Assessment of critical column parameters. Engineering Structures, 51, 188-199. https://doi.org/10.1016/j.engstruct.2013.01.017

Ozbakkaloglu, T., & Akin, E. (2012). Behavior of FRP-confined normal-and high-strength concrete under cyclic axial compression. Journal of Composites for Construction, 16(4), 451-463. https://doi.org/10.1061/(ASCE)CC.1943-5614.0000273

Ozbakkaloglu, T., & Vincent, T. (2014). Axial compressive behavior of circular high-strength concrete-filled FRP tubes. Journal of Composites for Construction, 18(2), 04013037. https://doi.org/10.1061/(ASCE)CC.1943-5614.0000410

Pham, T. M., & Hadi, M. N. S. (2014). Confinement model for FRP confined normal-and high-strength concrete circular columns. Construction and Building Materials, 69, 83-90. https://doi.org/10.1016/j.conbuildmat.2014.06.036

Pham, T. M., & Hao, H. (2016). Review of concrete structures strengthened with FRP against impact loading. Structures, 7, 59-70. https://doi.org/10.1016/j.istruc.2016.05.003

Pour, A. F., Ozbakkaloglu, T., & Vincent, T. (2018). Simplified design-oriented axial stress-strain model for FRP-confined normal-and high-strength concrete. Engineering Structures, 175, 501-516. https://doi.org/10.1016/j.engstruct.2018.07.099

Reglero Ruiz, J. A., Trigo-López, M., García, F. C., & García, J. M. (2017). Functional aromatic polyamides. Polymers, 9(9), 414. https://doi.org/10.3390/polym9090414

Rivandi, E., & Jamili Oskouie, R. (2024). A Novel Approach for Developing Intrusion Detection Systems in Mobile Social Networks. Available at SSRN 5174811. https://doi.org/10.2139/ssrn.5174811

Rochette, P., & Labossiere, P. (2000). Axial testing of rectangular column models confined with composites. Journal of Composites for Construction, 4(3), 129-136. https://doi.org/10.1061/(ASCE)1090-0268(2000)4:3(129)

Rong, C., & Shi, Q. (2018). Axial-strength model for FRP-confined concrete based on the improved twin shear strength theory. Composite Structures, 202, 102-110. https://doi.org/10.1016/j.compstruct.2017.12.020

Rousakis, T. C., Karabinis, A. I., Kiousis, P. D., & Tepfers, R. (2008). Analytical modelling of plastic behaviour of uniformly FRP confined concrete members. Composites Part B: Engineering, 39(7-8), 1104-1113. https://doi.org/10.1016/j.compositesb.2008.05.001

Rousakis, T. C., Rakitzis, T. D., & Karabinis, A. I. (2012). Design-oriented strength model for FRP-confined concrete members. Journal of Composites for Construction, 16(6), 615-625. https://doi.org/10.1061/(ASCE)CC.1943-5614.0000295

Saadatmanesh, H., Ehsani, M. R., & Li, M.-W. (1994). Strength and ductility of concrete columns externally reinforced with fiber composite straps. Structural Journal, 91(4), 434-447. https://doi.org/10.14359/4151

Sabzi, J., & Esfahani, M. R. (2018). Effects of tensile steel bars arrangement on concrete cover separation of RC beams strengthened by CFRP sheets. Construction and Building Materials, 162, 470-479. https://doi.org/10.1016/j.conbuildmat.2017.12.053

Sadeeq, H. T., & Abdulazeez, A. M. (2022). Giant trevally optimizer (GTO): A novel metaheuristic algorithm for global optimization and challenging engineering problems. Ieee Access, 10, 121615-121640. https://doi.org/10.1109/ACCESS.2022.3223388

Sadeghian, P., & Fam, A. (2015). Improved design-oriented confinement models for FRP-wrapped concrete cylinders based on statistical analyses. Engineering Structures, 87, 162-182. https://doi.org/10.1016/j.engstruct.2015.01.024

Shaikh, F. U. A., & Alishahi, R. (2019). Behaviour of CFRP wrapped RC square columns under eccentric compressive loading. Structures, 20, 309-323. https://doi.org/10.1016/j.istruc.2019.04.012

Shang, L., Isleem, H. F., Almoghayer, W. J. K., & Khishe, M. (2025). Prediction of ultimate strength and strain in FRP wrapped oval shaped concrete columns using machine learning. Scientific Reports, 15(1), 10724. https://doi.org/10.1038/s41598-025-95272-8

Shang, M., Li, H., Ahmad, A., Ahmad, W., Ostrowski, K. A., Aslam, F., Joyklad, P., & Majka, T. M. (2022). Predicting the mechanical properties of RCA-based concrete using supervised machine learning algorithms. Materials, 15(2), 647. https://doi.org/10.3390/ma15020647

Siddiqui, N. A., Alsayed, S. H., Al-Salloum, Y. A., Iqbal, R. A., & Abbas, H. (2014). Experimental investigation of slender circular RC columns strengthened with FRP composites. Construction and Building Materials, 69, 323-334. https://doi.org/10.1016/j.conbuildmat.2014.07.053

Silva, M. A. G. (2011). Behavior of square and circular columns strengthened with aramidic or carbon fibers. Construction and Building Materials, 25(8), 3222-3228. https://doi.org/10.1016/j.conbuildmat.2011.03.007

Stylianidis, P. M., & Petrou, M. F. (2019). Study of the flexural behaviour of FRP-strengthened steel-concrete composite beams. Structures, 22, 124-138. https://doi.org/10.1016/j.istruc.2019.07.012

Sun, X., Dong, X., Teng, W., Wang, L., & Hassankhani, E. (2024). Creation of regression analysis for estimation of carbon fiber reinforced polymer-steel bond strength. Steel and Composite Structures, 51(5), 509-527.

Suter, R., & Pinzelli, R. (2001). Confinement of concrete columns with FRP sheets. Proc., 5th Int. Conf. on Fibre Reinforced Plastics for Reinforced Concrete Structures, 793-802.

Suykens, J. A. K., & Vandewalle, J. (1999). Least squares support vector machine classifiers. Neural Processing Letters, 9, 293-300. https://doi.org/10.1023/A:1018628609742

Teng, J. G., Huang, Y. L., Lam, L., & Ye, L. P. (2007). Theoretical model for fiber-reinforced polymer-confined concrete. Journal of Composites for Construction, 11(2), 201-210. https://doi.org/10.1061/(ASCE)1090-0268(2007)11:2(201)

Tian, Z. (2020). Short-term wind speed prediction based on LMD and improved FA optimized combined kernel function LSSVM. Engineering Applications of Artificial Intelligence, 91, 103573. https://doi.org/10.1016/j.engappai.2020.103573

Toutanji, H., & Deng, Y. (2002). Strength and durability performance of concrete axially loaded members confined with AFRP composite sheets. Composites Part B: Engineering, 33(4), 255-261. https://doi.org/10.1016/S1359-8368(02)00016-1

Vincent, T., & Ozbakkaloglu, T. (2013). Influence of fiber orientation and specimen end condition on axial compressive behavior of FRP-confined concrete. Construction and Building Materials, 47, 814-826. https://doi.org/10.1016/j.conbuildmat.2013.05.085

Wang, W., Sheikh, M. N., Al-Baali, A. Q., & Hadi, M. N. S. (2018). Compressive behaviour of partially FRP confined concrete: Experimental observations and assessment of the stress-strain models. Construction and Building Materials, 192, 785-797. https://doi.org/10.1016/j.conbuildmat.2018.10.105

Wang, Y., & Wu, H. (2010). Experimental investigation on square high-strength concrete short columns confined with AFRP sheets. Journal of Composites for Construction, 14(3), 346-351. https://doi.org/10.1061/(ASCE)CC.1943-5614.0000090

Wang, Y., & Wu, H. (2011). Size effect of concrete short columns confined with aramid FRP jackets. Journal of Composites for Construction, 15(4), 535-544. https://doi.org/10.1061/(ASCE)CC.1943-5614.0000178

Wang, Y., & Zhang, D. (2009). Creep-effect on mechanical behavior of concrete confined by FRP under axial compression. Journal of Engineering Mechanics, 135(11), 1315-1322. https://doi.org/10.1061/(ASCE)0733-9399(2009)135:11(1315)

Watanabe, K., Nakamura, H., Honda, Y., Toyoshima, M., Iso, M., Fujimaki, T., Kaneto, M., & Shirai, N. (1997). Confinement effect of FRP sheet on strength and ductility of concrete cylinders under uniaxial compression. Proc., 3rd Int. Symp. on Non-Metallic (FRP) Reinforcement for Concrete Structures, 1, 233-240.

Wu, G., Wu, Z. S., Lu, Z. T., & Ando, Y. B. (2008). Structural performance of concrete confined with hybrid FRP composites. Journal of Reinforced Plastics and Composites, 27(12), 1323-1348. https://doi.org/10.1177/0731684407084989

Wu, H.-L., Wang, Y.-F., Yu, L., & Li, X.-R. (2009). Experimental and computational studies on high-strength concrete circular columns confined by aramid fiber-reinforced polymer sheets. Journal of Composites for Construction, 13(2), 125-134. https://doi.org/10.1061/(ASCE)1090-0268(2009)13:2(125)

Yang, H., Song, H., & Zhang, S. (2015). Experimental investigation of the behavior of aramid fiber reinforced polymer confined concrete subjected to high strain-rate compression. Construction and Building Materials, 95, 143-151. https://doi.org/10.1016/j.conbuildmat.2015.07.084

Yaychi, B. M., & Esmaeili-Falak, M. (2024). Estimating Axial Bearing Capacity of Driven Piles Using Tuned Random Forest Frameworks. Geotechnical and Geological Engineering, 42(8), 7813-7834. https://doi.org/10.1007/s10706-024-02952-9

Yin, H. (2025). Ultimate strain estimation of concrete wrapped by aramid fiber employing coati optimization-based systems. Multiscale and Multidisciplinary Modeling, Experiments and Design, 8(1), 1-17. https://doi.org/10.1007/s41939-024-00668-0

Zarei, M., Mohseni, F., & Sohrabi, P. (2024). Correlates of spatial structure variability in Bushehr port-city: A comprehensive analysis using fuzzy cognitive mapping methodology. J. Infrastruct. Policy Dev, 8, 8789. https://doi.org/10.24294/jipd.v8i11.8789

Zhang, K., Zhang, Y., & Razzaghzadeh, B. (2024). Application of the optimal fuzzy-based system on bearing capacity of concrete pile. Steel and Composite Structures, 51(1), 25.

Zhao, W., Wang, L., & Mirjalili, S. (2022). Artificial hummingbird algorithm: A new bio-inspired optimizer with its engineering applications. Computer Methods in Applied Mechanics and Engineering, 388, 114194. https://doi.org/10.1016/j.cma.2021.114194

Zhou, Y., Liu, X., Xing, F., Cui, H., & Sui, L. (2016). Axial compressive behavior of FRP-confined lightweight aggregate concrete: An experimental study and stress-strain relation model. Construction and Building Materials, 119, 1-15. https://doi.org/10.1016/j.conbuildmat.2016.02.180

Disclaimer